

The Direct DIVAM Experiment: A Spin Dynamics Analysis

Paul Hazendonk,^{*,†} Philip Wormald,[‡] and Tony Montana[†]

Department of Chemistry and Biochemistry, University of Lethbridge, Lethbridge, Alberta T1K 3M4, Canada, and School of Chemistry, University of St. Andrews, Purdie Building, St Andrews KY16 9ST, U.K.

Received: December 5, 2007; Revised Manuscript Received: March 30, 2008

Domain selection in polymer NMR is limited to experiments specifically suited to each structural domain owing to its particular spin dynamics and relaxation properties. The DIVAM experiment can be tuned to select for signal from the domain of interest, making it possible to obtain signals specific to different domains using only one experiment. An early description of this sequence explains this tunability using a simple one-spin-relaxation model, thereby limiting the selection mechanism to incoherent processes and thus ignoring the coherent terms such as chemical shift anisotropy (CSA), dipolar coupling and offset terms. Experiments have shown that when the DIVAM sequence is applied directly to the nucleus of interest, referred to as direct DIVAM (DD), transient behavior is observed in the signal intensity on the sample spinning time scale. This indicates that the coherent terms are involved in the selection process; the exact role of these terms is explored in this work. SIMPSON simulations illustrate that the CSA and offset terms can play a dominant role in domain selection; however, the dipole term was relatively ineffective and required large values before substantial selection was predicted. Using a one-spin-relaxation model, which now includes a chemical shift evolution term, an analytical expression for the signal intensity was provided as a function of interpulse delay (τ), excitation angle (θ), relaxation time (T_2), and offset frequency ($\Delta\nu$). These indicate that the selection behavior varies substantially with differing time scales and excitation angles. For small angles and long delay times DD behaves primarily as a relaxation filter, whereas for larger angles and short delay times the coherent terms take over dominated by the CSA interactions. The DD sequence can therefore be set to select on the basis of the transverse relaxation rate or the strength of the CSA interaction, depending on the excitation angle used.

Introduction

Overview. The discrimination induced by variable-amplitude minipulse (DIVAM) experiment has been shown to select for signal from mobile and disordered, or rigid and ordered domains, using the appropriate pulse angle and interpulse delay time.^{1,2} Previously a one-spin-relaxation model explained this selection behavior, where the proton z -magnetizations are filtered, followed by cross-polarization (CP) to another nucleus, which in most cases has been ^{19}F . Although this explanation seems to be satisfactory for the CP DIVAM experiment, it does not explain the behavior when the DIVAM filter is applied directly to the ^{19}F nucleus, also known as direct DIVAM (DD), with subsequent detection on ^{19}F .^{3,4} In this case, transient behavior in the signal intensity is observed with interpulse delay time as the excitation angle increases. This requires a more sophisticated explanation that takes into account the effects of both spin dynamics and relaxation.

This work provides a spin-dynamics investigation into the DD experiment, and the mode of domain selection will be explored. This sequence has been primarily applied to fluoropolymer systems; therefore some background is provided about this area to put the DIVAM method into context.

Fluoropolymers and ^{19}F NMR. Fluoropolymers are finding increased application in modern technology. Their use as nonstick coatings and components in durable textiles has made

products such as GORTEX and TEFLON household names.⁵ Fluoropolymers such as NAFION are used as membranes in polymer electrolyte membranes fuel cells (PEMFCs) for the production of innovative alternative fuel cells. Poly(vinylidene fluoride) (PVDF) sees widespread application in the electronics industry including loudspeakers, IR-detectors, and transducers exploiting its piezo- and pyro-electrical properties.^{6–8} Many proton containing fluoropolymers, such as PVDF, are semi-crystalline materials that exhibit polymorphism.^{9,10}

The fluorine nucleus has a long history in solid state NMR, where most work has been concentrated on perfluorinated materials.^{11,12} There are no inherent complications in performing solid-state experiments on these systems, because only a single high-band channel is required. This leaves out a large class of materials that contain both ^1H and ^{19}F , which would require probes capable of being tuned close in frequency while operating at high power. Probes with this capability became commercially available in the past decade and have sparked a new interest in these materials.

There are both advantages and disadvantages to using the ^{19}F nucleus. It is 100% abundant with a large gyromagnetic ratio, at 94% of ^1H . On the one hand, just like protons, it gives abundant signal and undergoes strong homonuclear coupling interactions. On the other hand, it is similar to carbon owing to its large chemical shift range, making it very sensitive to its immediate chemical environment, hence making it a useful structural probe. In addition, fluorine's strong homonuclear- and heteronuclear-couplings makes it possible to obtain useful structural information such as internuclear distances.¹³ The advantage of its large shift range is that it quenches much of

* To whom correspondence should be addressed. Phone: 403-329-2657. Fax: 403-329-2057. E-mail: paul.hazendonk@uleth.ca.

[†] University of Lethbridge.

[‡] University of St Andrews.

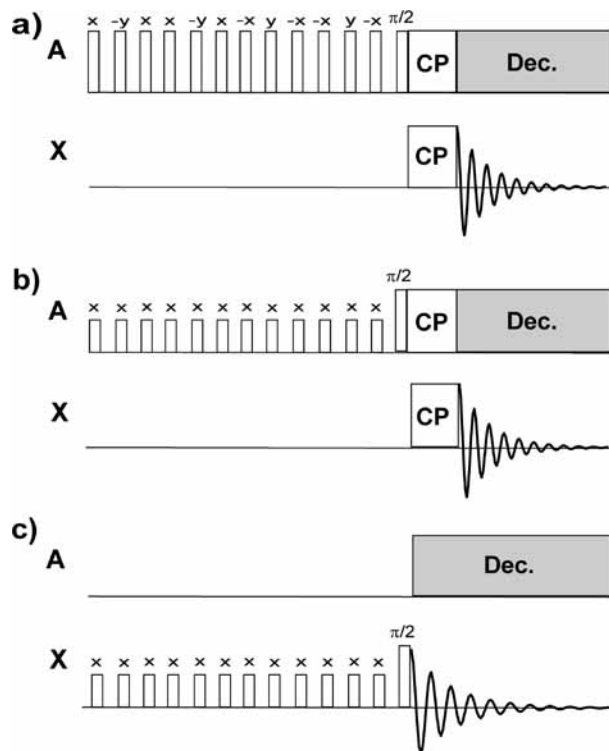


Figure 1. (a) Dipolar filter pulse sequence. (b) DIVAM pulse sequence. (c) Direct DIVAM pulse sequence

the spin diffusion between different signals, leading to high resolution at moderate spinning speeds, ca. 15 kHz, depending on the material. The heteronuclear couplings to protons are readily removed using multipulse decoupling sequences.^{14,15}

A major challenge in material science is obtaining structural details at the atomic level, from the various domains in semicrystalline materials. This is further complicated by the need to assemble information from various techniques, such as transmission electron microscopy, scanning electron microscopy, X-ray diffraction, dielectric spectroscopy, and differential scanning calorimetry, to form the structural picture, which is often not complete. Solid-state nuclear magnetic resonance spectroscopy (SSNMR) has been an invaluable tool, because it is able to determine useful information from all domains utilizing a suite of experiments, each able to select for signal specific to the chemical environments of interest.^{16–18} These methods exploit variations in spin-dynamics and relaxation, which are the result of differences in the structure and dynamics of the immediate environment of the nucleus. These experiments therefore give valuable insight into the behavior of these materials at the molecular level, which can be related to their macroscopic properties.¹⁹ Furthermore, this type of information is not typically available by the aforementioned traditional methodologies.

Historically SSNMR applications to polymeric materials has focused primarily on carbon spectroscopy combined with filtering schemes based on relaxation, dipolar, and chemical shift anisotropy interactions. Relaxation filters have been designed to select on the basis of T_1 , $T_{1\rho}$ and T_2 .^{16,20–23} Filtering methods exploiting the dipolar coupling interaction can be done using cross-polarization, dipolar dephasing and the dipolar filter (DF)^{24–32} (Figure 1a). Recent filters have also been designed using the CSA interaction, where signals with different chemical shift anisotropies were separated.³³ The CP DIVAM sequence is currently understood to select via a T_2 relaxation mechanism.

DIVAM Sequence. The DIVAM sequence,^{1–4} Figure 1b,c, is akin to the DF experiment being composed of a string of pulses separated by a fixed delay. However, unlike the DF, the pulse angles are not 90° and their phases remain constant throughout the sequence. A simple description of the signal nutation behavior invokes an on-resonance one-spin-relaxation model (Figure 2) that illustrates the behavior observed when filtering on proton with subsequent CP to, and detection on ^{19}F . Consider two components having significantly different transverse relaxation rates, where the first pulse rotates both components into the transverse plane. The component that relaxes slowly can be thought of as remaining essentially static during this delay period. In contrast, the rapidly dephasing component can be thought of as returning to the z-axis. With each subsequent pulse a difference in phase accumulates between the two components. Therefore, with the correct choice of excitation angle this phase difference can be 90° and effectively only one component is available to undergo CP. Optimum conditions for this sequence represent a carefully weighted balance between the excitation angle and the interpulse delay, maximizing selection while maintaining acceptable signal intensity. In this case no transient effects are seen with respect to the interpulse delay, as the results of spinning the sample, and a uniform phase is always observed in the fluorine spectrum.

This description is an oversimplification but works well when filtering on protons, as they have small CSA and isotropic terms. However, when the DIVAM sequence is applied directly to fluorine, without CP from proton, this description is no longer valid and the effects of coherent terms must be considered. The roles of both coherent evolution and relaxation in the selection observed in the Direct DIVAM experiment are investigated in the following treatment.

Experimental Section

Solid-State NMR Measurements. The fluoropolymer sample was α -PVDF (Kynar 301 F), supplied by Atofina, France, with a molecular weight of 1×10^6 by GPC, reverse unit content of 4.7% by NMR, crystallinity of $\sim 28\%$, and melting point of 158°C by DSC.⁷ All measurements were made on a Varian Inova 500 MHz NMR spectrometer operating at 470.18 MHz for the ^{19}F nucleus. A Varian 2.5 mm T3 triple channel HFX probe was used at ambient temperature 21°C with a MAS rate of 25 kHz. The 90° pulse was calibrated at $2.5\ \mu\text{s}$, and the excitation angles were arrayed in 2.5° steps from 0° to 90° by varying the radio frequency (RF) power. All pulses were centered on the amorphous peak of the PVDF spectrum. Two-pulse phase modulated (TPPM) decoupling was applied during fluorine acquisition. The spectral referencing was performed with C_6F_6 ($\delta_{\text{F}} = -166.4$ ppm with respect to the CFCl_3) and with ^1H decoupling, so that corrections for the Bloch–Siegert shift⁸ are not required. Zirconium oxide rotors were used with Vespel drive caps to avoid any fluorine background signal and the sample volume was restricted to $20\ \mu\text{L}$ to increase RF homogeneity.

The DIVAM sequence was performed using twelve $2.5\ \mu\text{s}$ pulses (pulse width (pw) = $2.5\ \mu\text{s}$), with RF centered on the amorphous signal of PVDF at -91.2 ppm, each separated by an interpulse delay (τ), and was terminated by a 90° observation pulse. All experimental measurements used a MAS rate of 25 kHz. A series of measurements were performed with $\tau = 3\ \mu\text{s}$ and the excitation angles arrayed as described earlier. Measurements were also made for a series of fixed excitation angles, while varying the interpulse delay. The interpulse delays were

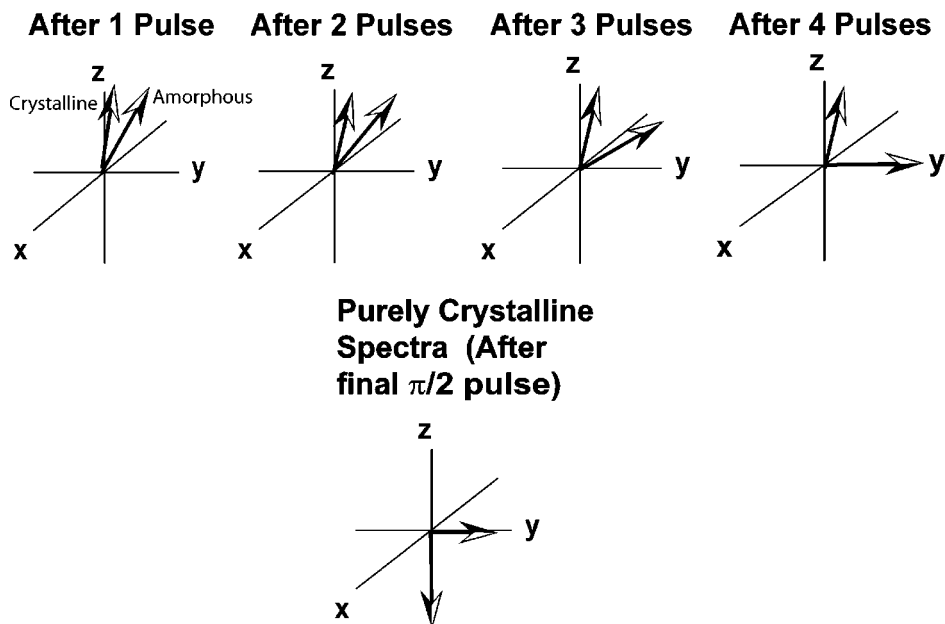


Figure 2. One-spin-relaxation description of the DIVAM experiment. A vector diagram of magnetization from the two domains, with differing T_2 relaxation times, under the operation of the DIVAM pulse train.

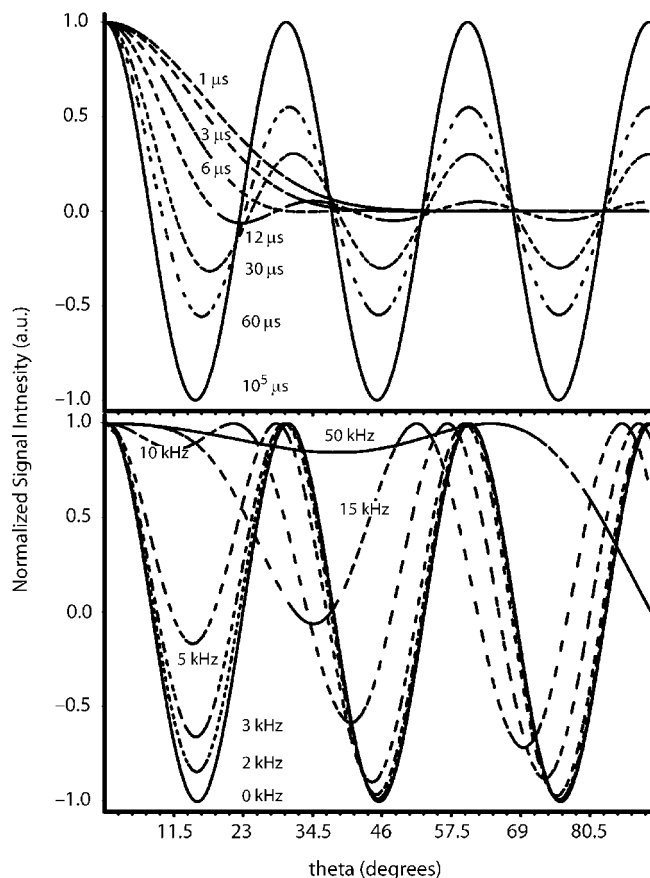


Figure 3. Maple simulations of the direct DIVAM sequence illustrating the effect of transverse relaxation (top) and simple chemical shift evolution term (bottom) on the nutation behaviour of the z -magnetization at the end of the sequence.

these curves do not change with T_2 , only their relative contributions do. These expressions predict that there will be different nutation behavior between components with differing relaxation rates, which forms the basis of a selection mechanism that will be explored further when discussing the experimental results on PVDF (see below).

A few of the curves from the bottom of Figure 3 were chosen and decomposed into their components, A_n (Figure 5) Notice that the contribution from each curve does not change substantially upon increasing the chemical shift; however, their shapes change dramatically, especially for the higher order terms. This illustrates that with each pulse-delay cycle a new component is added to the z -magnetization that has a unique dependency on the excitation angle as a result of chemical shift evolution during the interpulse delay. Also note that the higher order terms are essential to reproduce the correct shape of the nutation curves, especially at the higher excitation angles, and must be considered. These terms are the result of residual transverse components which, unless dephased by the end of the sequence, will lead to significant phase distortions in the spectra at larger excitation angles. These phase distortions are observed in the experimental DIVAM arrays for PVDF when short interpulse delays and large excitation angles are used (see the experiments on PVDF below).

To model the spin dynamics effects properly and to accurately reproduce the component curves, a full treatment including the offset, CSA and dipole terms needs to be included, along with relaxation, which is currently not practicable with available simulation software.

Simpson Simulations. Simulations of the DD sequence were performed by probing the effect of each term in the ^{19}F Hamiltonian separately. Parallel simulations were performed using ideal and real pulses, under rotor-synchronized and nonrotor-synchronized conditions. Figures 6–8 show these results. The nutation behavior of the z -magnetization remaining after the filter sequence is explained separately for each term in the Hamiltonian in the following text.

Isotropic Offset Term. The isotropic term (Figure 6A) shows that for small frequencies, ca. 10 kHz or less, nutation is observed at a rate of 12 times the excitation angle ($\cos(12\theta)$, as predicted), completing three full cycles by 90° . As the isotropic term increases, the nutation behavior changes dramatically and the amplitude of the first cycle decreases; however, its nutation frequency remains essentially unchanged, except for rather large values, ca. 15 kHz or greater. Furthermore, the first zero crossing, or null-point, of the

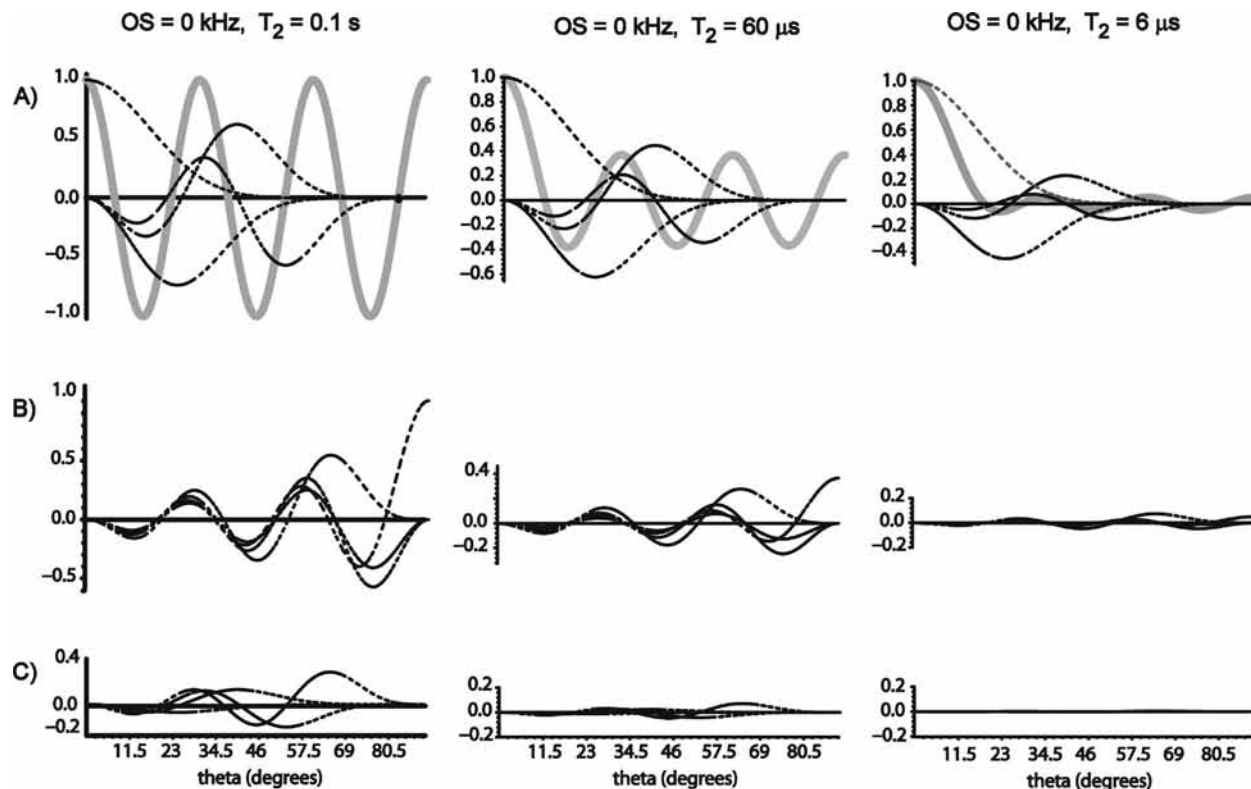


Figure 4. Selected nutation curves from the Maple simulations of the direct DIVAM sequence, considering only transverse relaxation, decomposed into components (A) A_0-A_3 , (B) A_4-A_7 , and (C) A_8-A_{11} for $T_2 = 0.1$ s, 60 μ s, and 6 μ s (the grey curves indicate the total nutation curves).

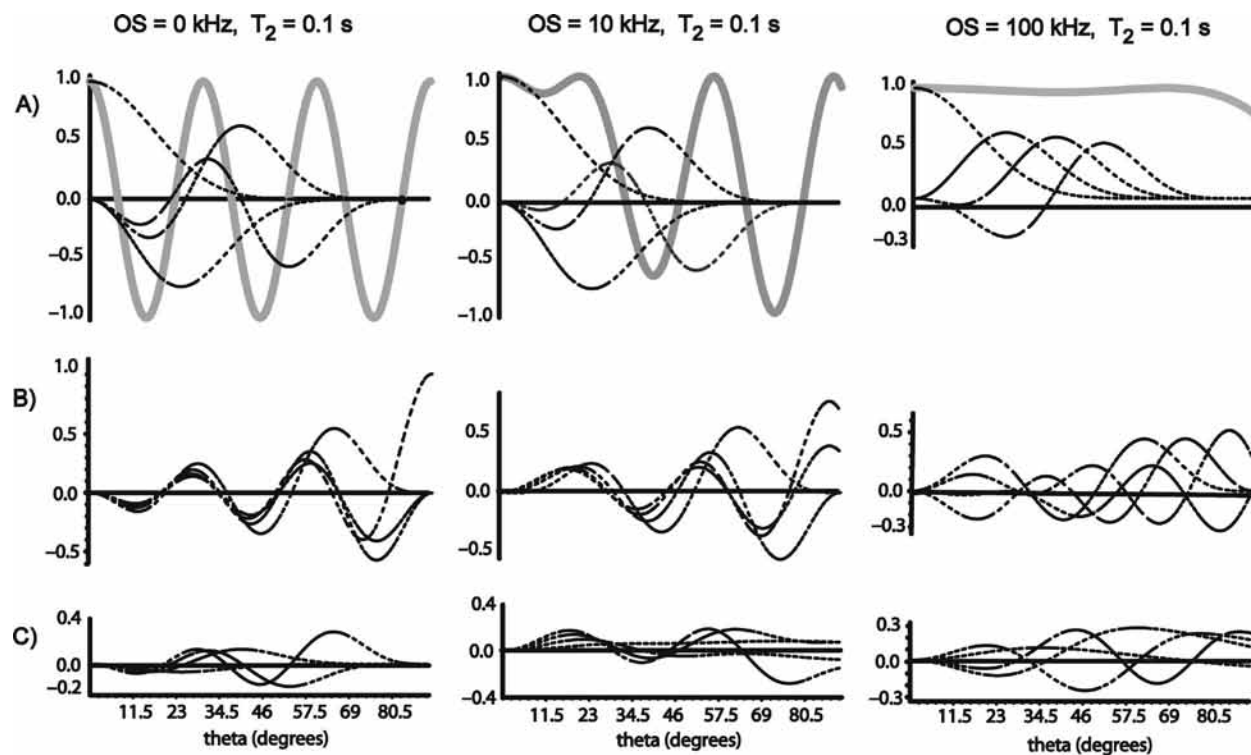


Figure 5. Selected nutation curves from the Maple simulations of the direct DIVAM sequence, considering only the chemical shift evolution term, decomposed into components (A) A_0-A_3 , (B) A_4-A_7 , and (C) A_8-A_{11} for $\Delta\nu = 0, 10,$ and 100 kHz (the grey curves indicate the total nutation curves).

z -magnetization increases with increasing offset, and hence selection can be achieved via this term. The Simpson simulations of the isotropic offset term are very similar to the results seen for chemical shift evolution in the analytical expression section (Figure 3 bottom), as expected. One should

note, however, that the DIVAM sequence is used to discriminate between overlapping signals, hence differences in isotropic frequency are not of interest, unless overlap from sideband signals is significant and cannot be avoided. No difference is observed between the rotor synchronized and

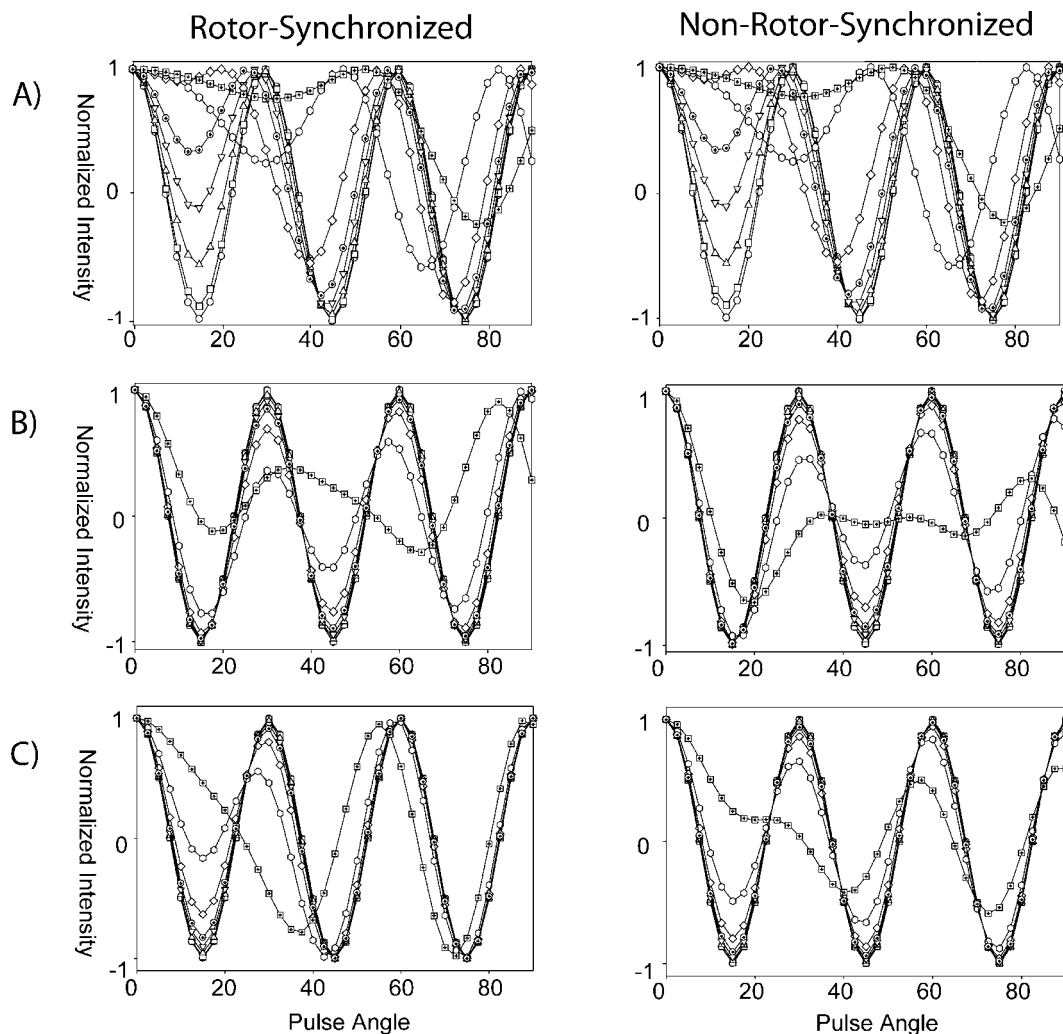


Figure 6. Simulation of the direct DIVAM sequence illustrating the behaviour of the (A) isotropic offset, (B) chemical shift anisotropy and (C) dipolar coupling terms in the Hamiltonian using real pulses. Each Hamiltonian term was varied between 1 and 50 kHz, where \circ = 1000 Hz, \square = 2500 Hz, \triangle = 5000 Hz, ∇ = 7500 Hz, \oplus = 10000 Hz, \diamond = 15000 Hz, \circ = 25000 Hz, and \boxtimes = 50000 Hz. These simulations used a pulse width of 1 μ s and an interpulse delay of 3.167 μ s. The rotor synchronized and nonrotor synchronized simulations used MAS rates of 20 and 25 kHz, respectively.

nonsynchronized cases, which is also to be expected, as the isotropic term is not affected by sample rotation.

The Chemical Shift Anisotropy Term. Simulations with the CSA term (Figure 6B) predict very different nutation behavior than those with the isotropic term. Most of the first nutation cycle is insensitive to the size of the CSA interaction until the first maximum, at 30°, where the z -magnetization is significantly reduced for values greater than 25 kHz. Beyond this point the amplitude of nutation is attenuated until the end of the third cycle. These nutation curves show that selection is possible by the CSA term, because for values greater than 25 kHz, the first zero-crossing shifts to larger excitation angles than those seen for smaller values. This implies that in this case for ^{19}F nuclei a minimum difference in CSA of 50 ppm is required for selection via the CSA term.

When DD is not rotor synchronized, the differences in behavior are further complicated due to the orientational dependency of the CSA term. In this case, the nutation behavior (Figure 6B right) shows similar but more complex behavior when compared to the rotor synchronized case; however, essentially the same observations can be made. Selections can be achieved for CSA values 50 kHz and larger, and the nutation amplitude beyond the first cycle is also reduced for values of

25 kHz and greater. Note that at low excitation angles the selection behavior is somewhat compromised, as there is less variation in the zero-crossing point with increasing CSA values; therefore, for optimum selection performance it would be best to employ rotor synchronization.

The effects of rotor synchronization were explored further using real pulses for a large and a small CSA value over a series of interpulse delays at a spinning speed of 20 kHz (Figure 7). Rotor synchronization occurs at $\tau = 3 \mu\text{s}$, corresponding to $T_F = 48 \mu\text{s}$, where a maximum difference is seen between the two curves at $\theta = 15^\circ$, indicating the optimum selection conditions. Notice that the selection conditions remain favorable beyond $\tau = 3 \mu\text{s}$, which suggests that rotor synchronization, with respect to T_F , is important for short delays; however, beyond the first rotor period synchronization is less essential.

Dipolar Coupling Term. The nutation curves for the dipolar term (Figure 6C) have similarities with the curves for both the isotropic and CSA terms; however, when the dipolar term reaches 50 kHz, the angle at which the first zero-crossing occurs shifts to an excitation angle that is much larger than what was seen for the CSA term (Figure 6B). Furthermore, much like the isotropic term the amplitude of oscillation after the first minimum, at 15°, decreases as the dipole couplings increase. It

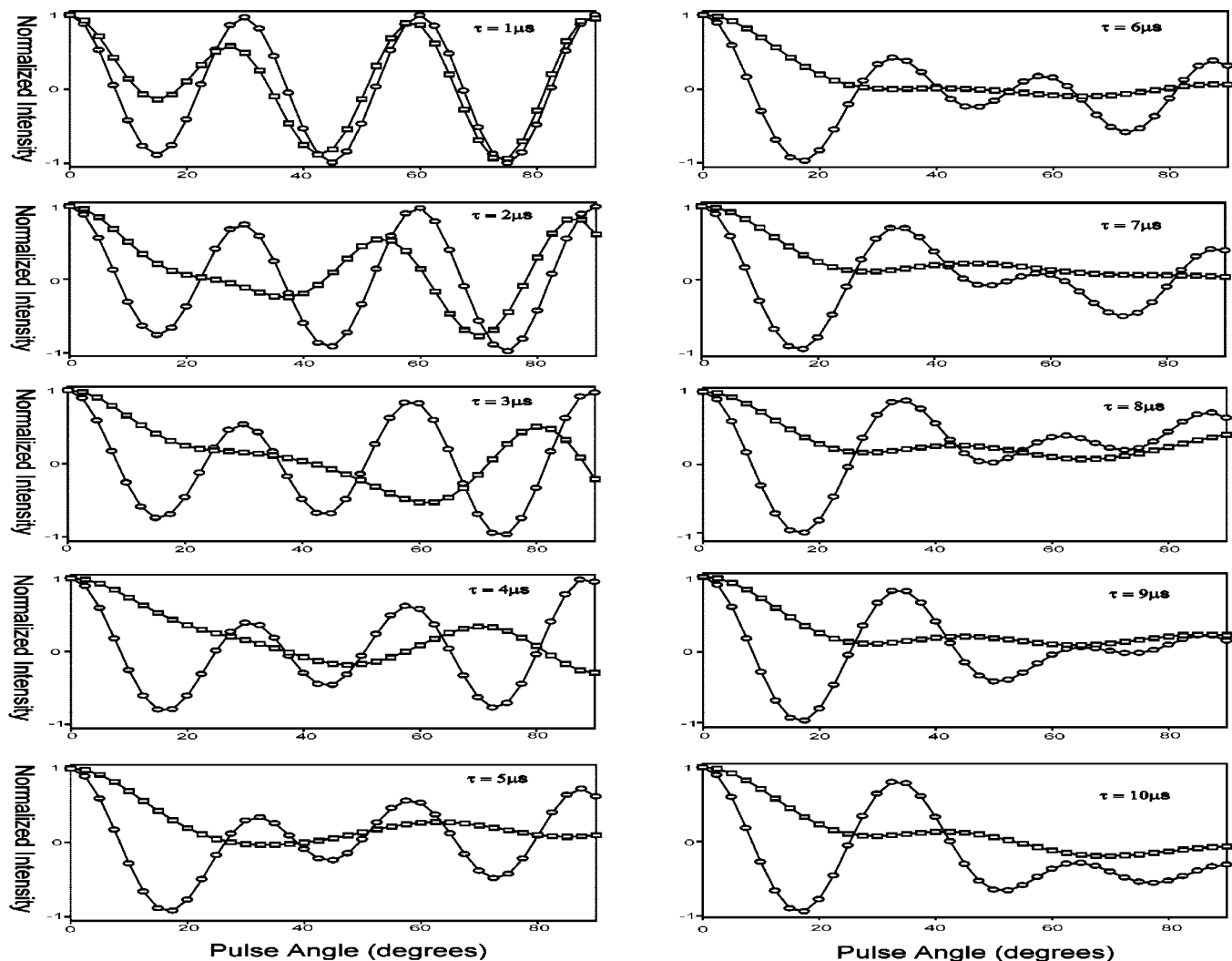


Figure 7. Effect of rotor-synchronization on the selectivity of the Direct DIVAM pulse sequence for various chemical shift anisotropy and intersample delay values, using real pulses where $\circ = 25$ kHz and $\square = 90$ kHz. A MAS rate of 20 kHz and a pulse width of $1 \mu\text{s}$ were used.

is important to note that, to achieve selection, a dipolar interaction greater than 25 kHz is required. For fluoropolymer systems, dipolar couplings of this size are uncommon; consequently, the dipolar term is not expected to significantly impact the selection behavior. On the other hand, the dipolar terms can play a significant role in domain selection in materials with much less internal mobility where larger dipolar couplings would be expected between strong abundant spins. When DD is not rotor synchronized, the dipolar term, just like the CSA term, is even less able to cause selection as the zero-crossing points are more closely spaced than for the rotor synchronized case. In this case (Figure 6C right), a dipolar coupling of at least 50 kHz is required to achieve selection.

Figure 8 shows a series of simulations for the dipole term over a range of intersample delays for three dipole-coupling values, which bares a close resemblance to the corresponding simulations for the CSA term. Rotor synchronization occurs near $\tau = 3 \mu\text{s}$, corresponding to $T_F = 48 \mu\text{s}$, where optimum discrimination conditions are achieved at $\theta = 15^\circ$ between the 10 and 90 kHz curves. As before, rotor synchronization is less important for a T_F larger than one rotor period. On the one hand, for all delay times considered, no efficient selection could be attained between the 10 and 25 kHz curves at the first zero crossing. On the other hand, these simulations do suggest that selection between these two curves could take place for larger excitation angles, such as $\theta = 30^\circ$ and $\theta = 60^\circ$, and for larger

delays, ca. $\tau = 7\text{--}10 \mu\text{s}$. Currently, the DIVAM sequence is typically implemented with short delay times, consequently the dipole term cannot be expected to have a significant effect on the selection process.

Experimental Observations of Direct DIVAM Applied to PVDF. Figure 9 shows the ^{19}F spectra of PVDF acquired at an MAS rate of 25 kHz under ambient conditions. The signal from the amorphous domain is a narrow intense line in the center of the spectrum, at -91.2 ppm. The two crystalline signals appear as broad shoulders on each side of the amorphous peak at -82.1 and -95.6 ppm.⁷ A third broad signal, composed of two overlapping lines of low intensity, near -118 ppm corresponds to the defects units (D), which are due to the reverse addition monomer units, giving rise to adjacent CF_2 groups. Figure 10 shows a series of ^{19}F DD spectra, measured over a range of excitation angles from 0 to 90° with an intersample delay of $3 \mu\text{s}$, illustrating the nutation behavior of the various signals in the spectrum of PVDF during the DD sequence. Notice that the amorphous signal nutates at a rate of 12 times the excitation angle, and that the rate of the crystalline signal is slower. This is particularly striking near 15° where the amorphous signal passes through a null condition, and that of the crystalline signal still has significant positive intensity and does not appear to cross zero until 60° . For larger excitation angles the simple nutation behavior seems to break down markedly for the crystalline signal. The two crystalline peaks are offset with

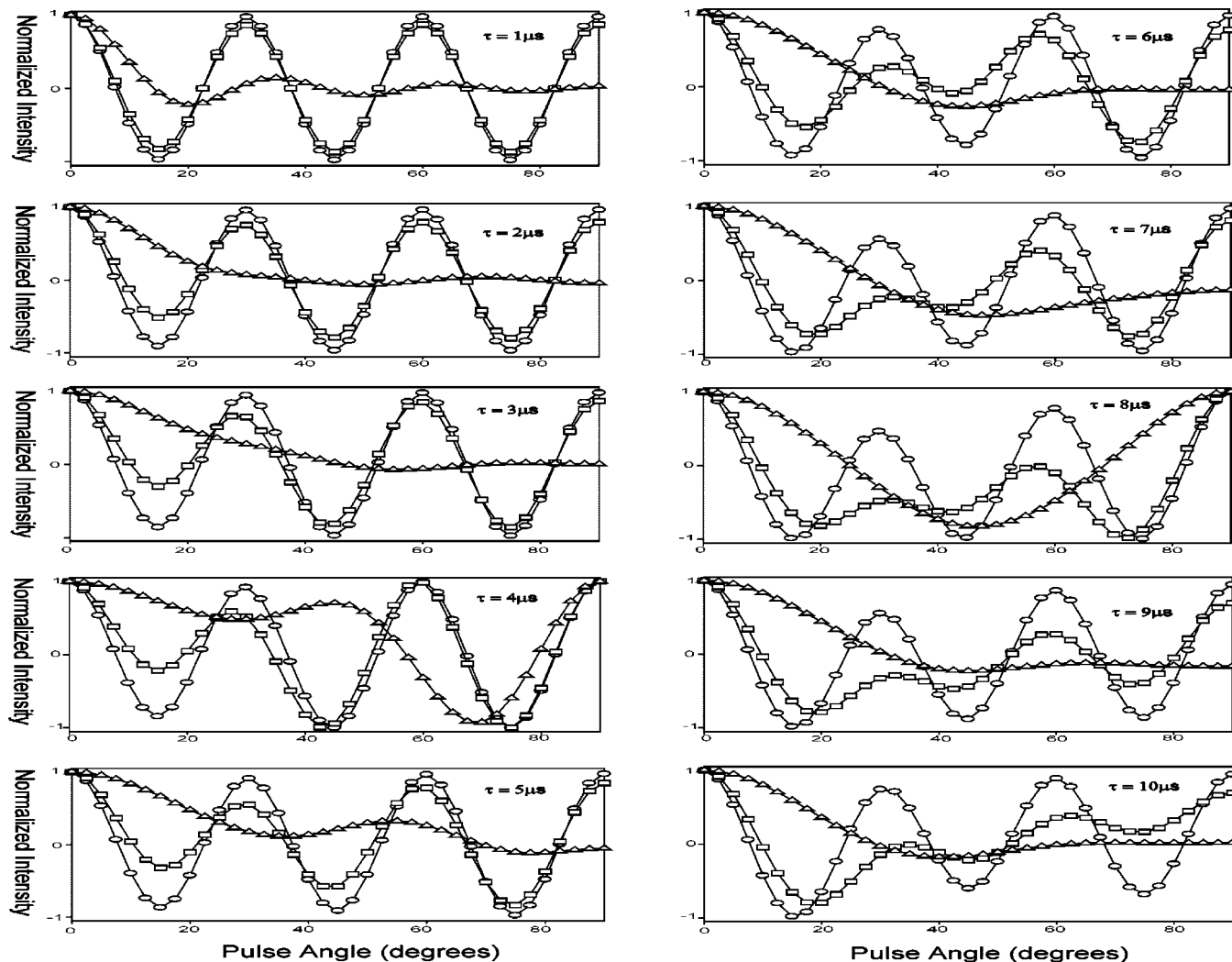


Figure 8. Effect of rotor-synchronization on the selectivity of the Direct DIVAM pulse sequence for various dipolar coupling and interpulse delay values, using real pulses where $\circ = 10$ kHz, $\square = 25$ kHz, and $\triangle = 90$ kHz. A MAS rate of 20 kHz and a pulse width of $1 \mu\text{s}$ were used.

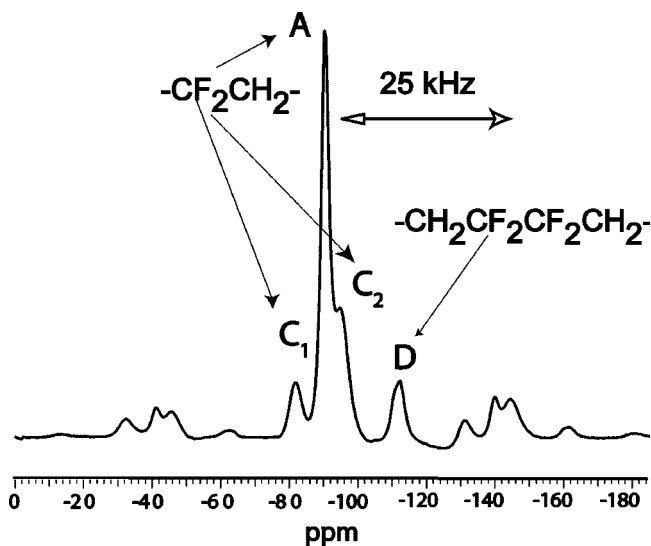


Figure 9. DP ^{19}F MAS NMR spectrum of PVDF at 25 kHz under ambient conditions with the RF centered on the amorphous peak.

respect to the amorphous signal, differing by 7 kHz, which causes a significant deviation in their nutation rates, which is consistent with predictions made by the isotropic offset simulations (Figure 6A) and the analytical expressions (Figure 3 bottom).

In Figures 11 and 12 a series of DD experiments are shown where the interpulse delay was varied while keeping the excitation angle fixed. To give insight into the selection behavior on different timescales, a short and a long time series was considered for selected excitation angles. In Figure 11 the delay time varied such that the T_F ranges over approximately two rotor periods (T_R) in steps of $3/4 T_R$, and in Figure 12 the delay time varied such that the T_F covered 2400 rotor periods on a nonlinear scale, somewhat logarithmic in nature, with spacing increasing from 3, 6, 15, 150 to 300 T_R .

Considering the short time series, for a small excitation angle, little transient behavior is seen. For example, in the 2.5° series (Figure 11 bottom row) the signal intensity does not vary with delay time. Also note in the 15° series (Figure 11 second from bottom) the amorphous signal is near its first null condition, its intensity being mostly suppressed, whereas the crystalline signal is only somewhat smaller than it was initially. In this case both signals show little variation in signal intensity on the short time scale. Beyond 30° the variations in signal intensities with rotor phase become increasingly evident. Considering 60° and higher the amorphous signal clearly passes through nearly two complete cycles (Figure 11). The same oscillations are seen in the crystalline signals but are less dramatic.

The long time series reflects the time scale of T_2 for PVDF, which along with their corresponding T_1 values are tabulated in

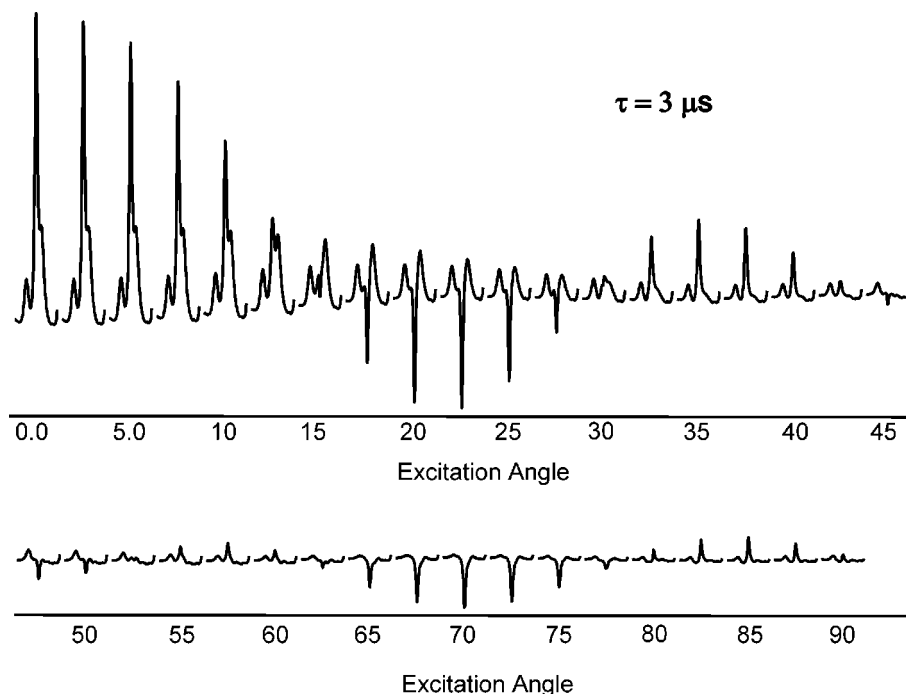


Figure 10. ^{19}F direct DIVAM spectra of PVDF over a series of excitation angles with an interpulse spacing of $3\ \mu\text{s}$, pulse width of $2.5\ \mu\text{s}$, and a MAS rate of $25\ \text{kHz}$.

Table 1, where the interpulse delay ranges from 0.12 to 32 times T_2 for the amorphous signal, and from 0.40 to 100 times T_2 for the crystalline signals. For the small excitation angles, ca. 2.5° (Figure 12), the amorphous and crystalline signal remain unchanged as they experience little net rotation. For short delay times, as the excitation angles increases, their net rotation increases, reducing their intensity until they reach their first null condition; however, as the delay time increases, they recover intensity when exceeding the T_2 time scale. Beyond 30° the saturation effect becomes increasingly pronounced, eventually reaching a point at which the signal does not recover over the entire time range.

In summary, the long and the short time series illustrate two aspects of the spin dynamics during the DD experiment as the excitation angle is increased. The short time series shows that transient oscillations are observed only for the larger excitation angles. The long time series illustrates that the saturation effect is more pronounced with increasing excitation angle, which for long delay times recovers on the T_2 time scale. Both behaviors suggest that the transverse components play an important role in the spin dynamics and cannot be ignored.

To explain the role of the transverse components in the spin dynamics, let us return to the analytical expressions, equation 3, for a sequence limited to two pulse-delay cycles, for simplicity. Considering both relaxation and chemical shift evolution, while ignoring spin–lattice relaxation, \mathbf{I}_z will undergo the following transformation:

$$\begin{aligned} \mathbf{I}_z \xrightarrow{\theta_x - \tau - \theta_x - \tau} & \mathbf{I}_z [\cos^2 \theta - \sin^2 \theta \cos \omega t \exp(-\tau/T_2)] + \\ & \mathbf{I}_x \sin \theta \exp(-\tau/T_2) \sin \omega t \{ \cos \theta [1 + \cos \omega t \exp(-\tau/T_2)] + \\ & \cos \omega t \exp(-\tau/T_2) \} + \mathbf{I}_y \sin \theta \exp(-\tau/T_2) \times \\ & \{ -\cos \theta \cos \omega t [1 + \cos \omega t \exp(-\tau/T_2)] + \\ & \sin^2 \omega t \exp(-\tau/T_2) \} \quad (4) \end{aligned}$$

where ω depends parametrically on the spinning rate (ω_R), the chemical shift tensor and dipolar coupling tensor.

On the extreme end of the long time scale all the exponential terms disappear, and thus the transverse components can be removed, leaving the following expression for the longitudinal component:

$$\mathbf{I}_z \xrightarrow{\theta_x - \tau - \theta_x - \tau} \mathbf{I}_z \cos^2 \theta \quad (5)$$

This is the expression for the nutation behavior when relaxation dominates, where the signal saturates with increasing excitation angle, which is analogous to that shown in Figure 3 (top) for the twelve-pulse sequence. Hence for very long delay times the relaxation mechanism will determine selection. Note the signal intensity contains no time dependence; in other words, no transient behavior is expected on the rotor time scale and all dependencies on the chemical shift have been removed.

On an intermediate time scale, the first-order exponentials can be retained and the second-order terms are ignored, giving the expression

$$\begin{aligned} \mathbf{I}_z \xrightarrow{\theta_x - \tau - \theta_x - \tau} & \mathbf{I}_z [\cos^2 \theta - \sin^2 \theta \cos \omega t \exp(-\tau/T_2)] + \\ & \mathbf{I}_x \sin \theta \cos \theta \sin \omega t \exp(-\tau/T_2) - \\ & \mathbf{I}_y \sin \theta \cos \theta \cos \omega t \exp(-\tau/T_2) \quad (6) \end{aligned}$$

In this case more complex behavior is predicted and is indeed observed. Consider the case of small excitation angles, ca. 15° or less, where $\sin^2 \theta$ can be considered small enough to be ignored. This means that the second term of the longitudinal component falls away, leaving the $\cos^2 \theta$ dependence, as seen for extremely long delay times. In the vicinity of $\theta = 15^\circ$, where $\sin^2 \theta$ would no longer be considered negligible, this behavior is expected to persevere as the second term is further reduced owing to its $\exp(-\tau/T_2)$ dependence. The transverse components can also be ignored for small angles as they depend on $\sin \theta$, and are also further attenuated by relaxation due to their $\exp(-\tau/T_2)$ dependence. Again, it appears as if the relaxation mechanism dominates the

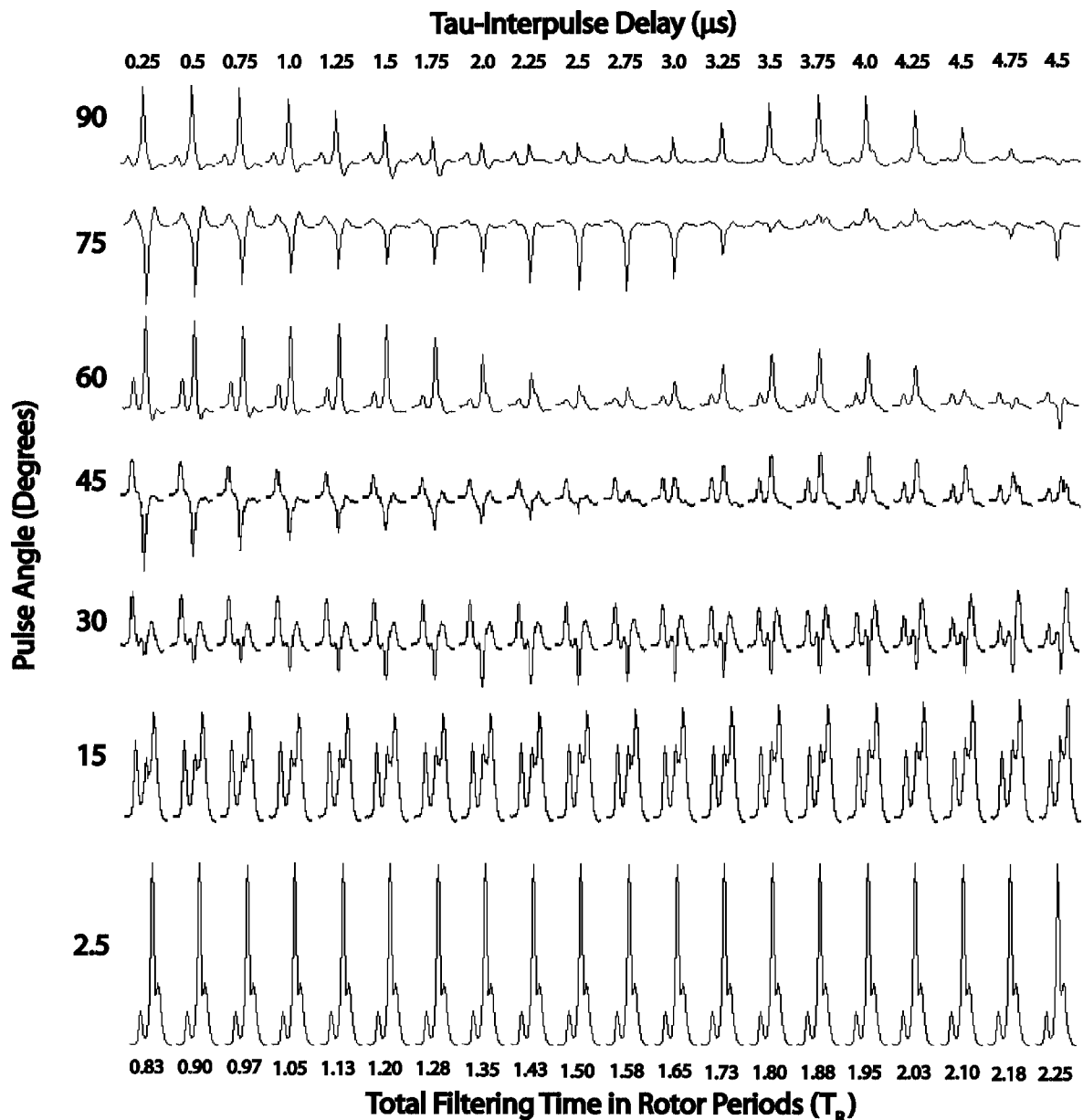


Figure 11. ^{19}F direct DIVAM spectra of PVDF over a series of interpulse delays, calibrated such that T_F covers 0–2 rotor periods (T_R). This array is shown for selected excitation angles from 2.5 to 90° using a MAS rate of 25 kHz and a pulse width of 2.5 μs .

selection process, as no transient oscillations are predicted with sample rotation, and no phase distortions are predicted, as the transverse components are lost. This behavior is observed experimentally for angles up to 15° for both time series (Figures 11 and 12), as the small angle approximation also holds true in the case of the short time scale.

For excitation angles greater than 15° these approximations begin to break down and the full expression in eq 6 has to be considered. Note that the resulting longitudinal component is made of two terms: the first term originates from the initial longitudinal component, which is time independent, and the second term is derived from the transverse magnetization, which has a time dependence determined by both T_2 and the chemical shift. This second term accounts for the recovery observed in the signal with increasing delay time (Figure 12) for intermediate angles where the signal only partially saturates. It decreases in magnitude with increasing τ , resulting in a net increase in the signal intensity on the time scale determined by the transverse relaxation rate, eventually leading to the form seen in eq 5.

This recovery behavior, observed experimentally (Figure 12), is reproduced using the analytical expressions, shown in Figure 13A, where the longitudinal component was computed as a function of $\log \tau$ for a long (L, typical of the amorphous domain) and short (S, typical of the crystalline domain) transverse relaxation time, covering delay times from 1 μs to 10 ms. Initially, the longitudinal magnetization experiences a net rotation of 12 times the excitation angle. As the delay time increases the effects of relaxation emerge, causing the net rotation to appear to decrease by the start of the long time scale. When the relaxation effect becomes more pronounced, which occurs over the long time scale, the signal eventually returns to an intensity reflecting the saturated state, defined by $\cos^{12} \theta$, thus for larger angles the signal is lost to saturation. For the long relaxation time (L), covering the entire time range, the calculations predict (i) at 2.5°, there is little net rotation at the start of the long time scale and hence no recovery is expected, (ii) at 15°, there is a large net rotation, approaching 120° at the start of the long time scale, allowing for significant recovery to an intensity of $\cos^{12}(15^\circ) = 0.66$, (iii) at 30°, there is a net

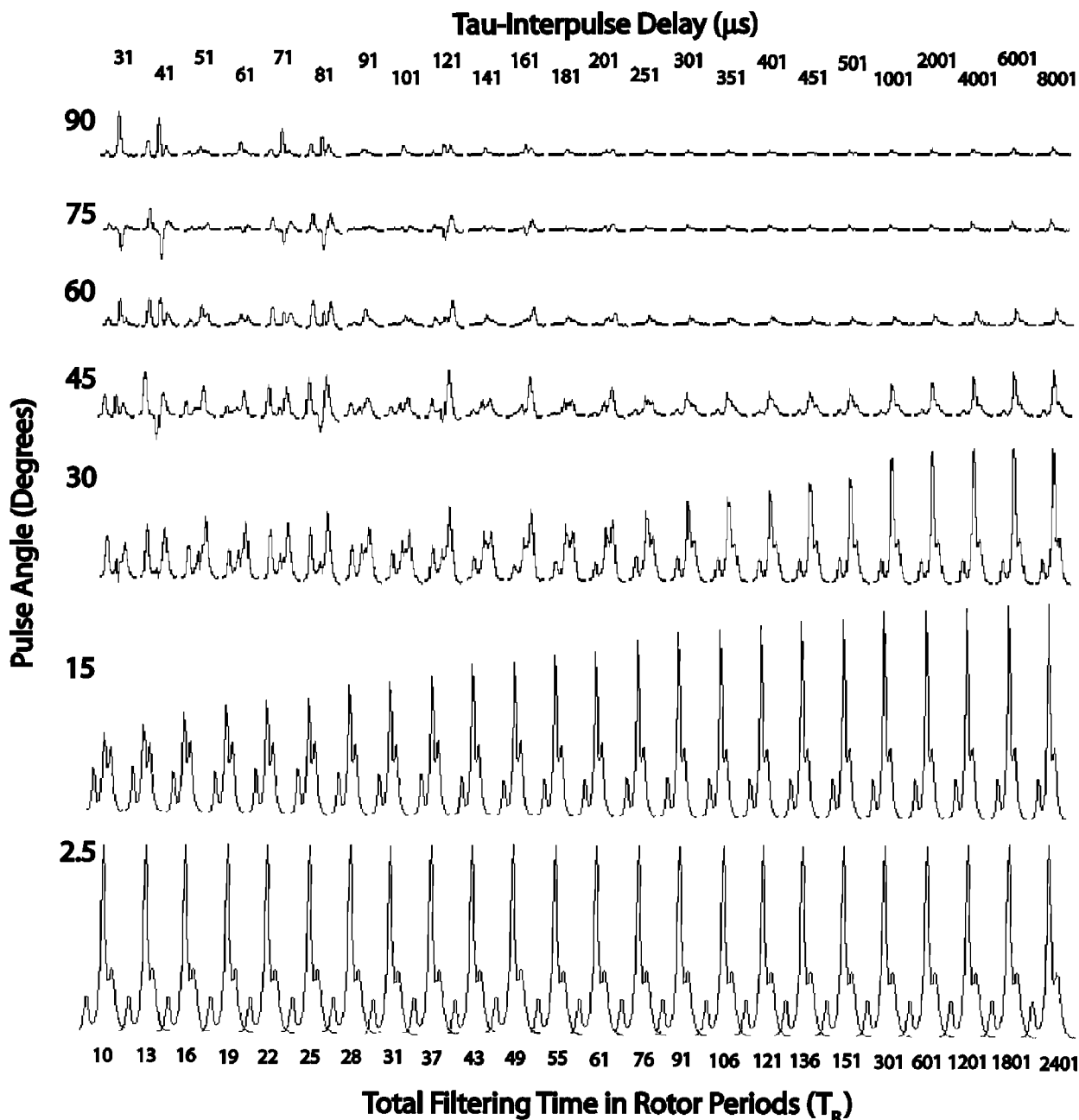


Figure 12. ^{19}F direct DIVAM spectra of PVDF over a series of interpulse delays, calibrated such that T_F covers 3–2400 rotor periods (T_R). This array is shown for selected excitation angles from 2.5 to 90° using a MAS rate of 25 kHz and a pulse width of 2.5 μs .

TABLE 1: Relaxation Measurements of $T_1(\text{F})$ by Inversion Recovery and $T_2(\text{F})$ by a Hahn-Echo, Both Using Proton Decoupling during Acquisition

	T ($^\circ\text{C}$)	C_1	C_2	A	D_1	D_2
$T_1(\text{F})$ (s)	60	0.63	N/A	0.57	0.59	0.59
$T_2(\text{F})$ (μs)	60	79.7	135.6	250.6	251.0	289.1

rotation near 300° at the start of the long time scale, which by the end reaches an intensity of $\cos^2(30^\circ) = 0.18$, reflecting significant saturation, and (iv) at 45° , it experiences a net rotation near 480° at the beginning of the long time scale and remains almost completely saturated until the end, with an intensity of 0.015. For the more rapidly relaxing component the same behavior is seen but shifted to a time scale commensurate with the difference in relaxation rates. As a result, for relaxation times typical of the crystalline domain and over much of the long time scale, the signal has already recovered to its fullest extent

at each excitation angle considered; hence a less pronounced change in intensity is observed.

For the short to intermediate time scales, and for angles greater than 15° , eq 6 predicts transient oscillations determined by the rotor period. These are observed on the short time scale (Figure 11) where the following expression holds:

$$\begin{aligned} \mathbf{I}_z \xrightarrow{\theta_x - \tau - \theta_x - \tau} & \mathbf{I}_z [\cos^2 \theta - \sin^2 \theta \cos \omega t] + \\ & \mathbf{I}_x \sin \theta \sin \omega t [\cos \theta (1 + \cos \omega t) + \cos \omega t] + \\ & \mathbf{I}_y \sin \theta [-\cos \theta \cos \omega t (1 + \cos \omega t) + \sin^2 \omega t] \quad (7) \end{aligned}$$

Recall that ω is a periodic function in time that depends on crystallite orientation with respect to the magnetic field, which can be stated in the general form:

$$\omega(t, \alpha, \beta, \gamma) = \omega_0 + \omega_1(\alpha, \beta) \cos(\omega_r t + \gamma) + \omega_2(\alpha, \beta) \cos(2\omega_r t + \gamma) \quad (8)$$

where α , β and γ are the Euler angles defining the crystallite orientation, ω_r is the spinning rate, ω_0 is the isotropic frequency, and ω_1 and ω_2 are dependent on the chemical shift and dipolar tensors according to expressions given elsewhere.³⁷ When the delay period is rotor synchronized the normal nutation behavior is predicted, including the effect of the isotropic frequency, as in Figure 3 (bottom) and 6A for the twelve pulse case. Otherwise, the intensity of the signal will depend on rotor phase, giving rise to oscillations in the signal intensity as seen in Figure 11 and illustrated in Figure 7 and 8 for the CSA and dipolar simulations, respectively.

In Figure 13B is shown two series of simulations based on the analytical expressions (eq 3), where an isotropic chemical shift (CS) term either is included along with relaxation or is not included (R). Note that on the long time scale the same

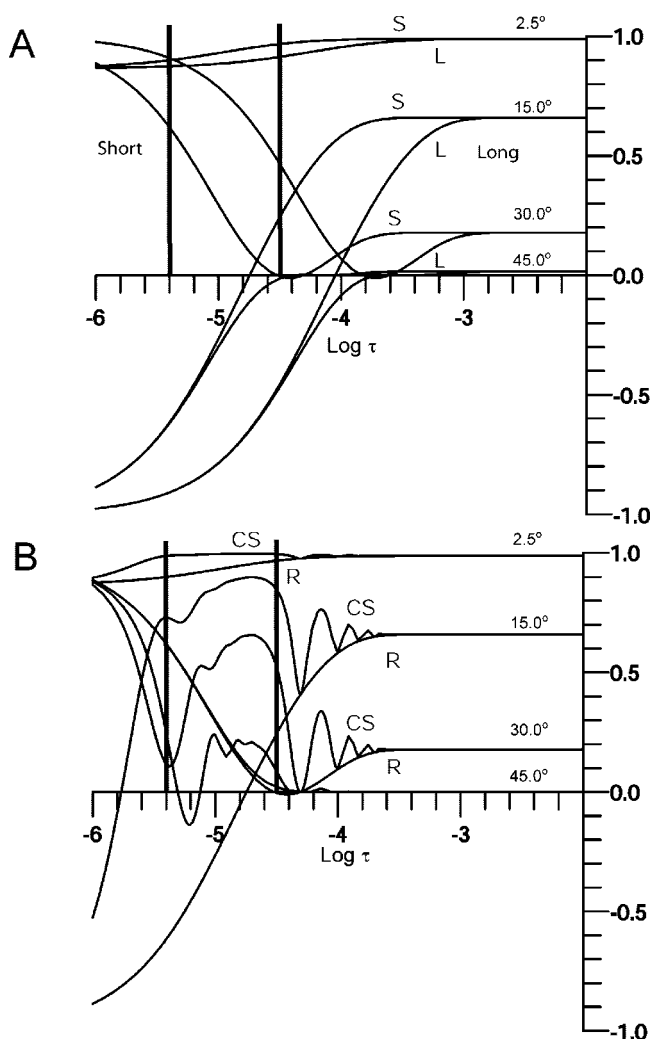


Figure 13. Maple simulations of the direct DIVAM sequence illustrating the effect of spin–spin relaxation rates and chemical shift evolution over the long and the short delay time regimes for selected excitation angles corresponding to Figures 11 and 12. (A) Comparison between the longitudinal magnetization remaining after the DIVAM filter as a function of $\log \tau$ for a long (L), 250 μs , and a short (S), 50 μs , spin–spin relaxation time without considering chemical shift evolution. (B) Comparison between the longitudinal magnetizations remaining after the DIVAM filter in the presence (CS) and absence (R) of a significant chemical shift interaction (20 kHz) as a function of $\log \tau$ for the short spin–spin relaxation time.

saturation and recovery behavior is seen for all the excitation angles as in Figure 13A. Observe that the dynamics is dominated by the chemical shift term over the short time scale leading into the long time scale, ca. $\log \tau = -5.5$ to $+4$, particularly for excitation angles 15° and 30°. The same behavior is seen experimentally for excitations angles of 30° and larger where the crystalline signal exhibits similar dynamics (Figure 12).

It is important to note that eq 6 predicts the emersion of phase distortions in the spectra for angles greater than 15° and short delays. This is the result of the transverse components being neither dampened by the $\sin \theta$ term nor dephased by transverse relaxation. The phase distortions predicted by these remaining transverse terms are observed experimentally where at large angles the nutation behavior is seen to be compromised (Figure 10). These phase distortions are also seen in the short time series (Figure 11) for angles greater than 30°. New strategies need to be devised that will remove these phase distortions such that DIVAM may be utilized for large angles and short delays.

Conclusions

(1) Direct DIVAM experiments performed with varying interpulse delays over the sample spinning time scale show transient behavior which was not seen in the original CP DIVAM experiment.

(2) Spin dynamics simulations illustrate that all three terms in the Hamiltonian, offset, CSA and dipole, can give rise to selection behavior; however, they predict that for fluoropolymer systems the CSA term dominates the DD selection behavior.

(3) Analytical expressions for the DD sequence show that for small excitation angles, as well as for long interpulse delays, the selection is driven by relaxation. For large excitation angles over the short and intermediate time scale, the effect of the coherent terms dominate the spin dynamics and phase distortions were predicted and observed.

(4) In principle, the DIVAM filter has two modes of operation where it can switch between selection on the basis of relaxation and coherent spin dynamics by choosing the appropriate excitation angle and interpulse delay. Application of DIVAM in the latter selection mode would greatly benefit from the removal of the phase distortions. This will be the subject of a future publication.

Acknowledgment. We acknowledge the assistance and expertise of Guangxin Lin and Dinu Iuga and the support of NSERC, CFI, ANPI and the U of L in this research. We also thank Nicole Andres and Jared Nieboer for assistance in the simulations and deconvolution.

References and Notes

- (1) Hazendonk, P.; Harris, R. K.; Ando, S.; Avalle, P. *J. Magn. Reson.* **2003**, *162*, 206–216.
- (2) Ando, S.; Harris, R. K.; Holstein, P.; Reinsberg, S. A.; Yamauchi, K. *Polymer* **2001**, *42*, 8137–8151.
- (3) Hazendonk, P.; deDenus, C.; Iuga, A.; Cahoon, P.; Nilsson, B.; Iuga, D. *J. Inorg. Organomet. Polym. Mater.* **2006**, *16*, 343–357.
- (4) Borisov, A. S.; Hazendonk, P.; Hayes, P. *J. Inorg. Organomet. Polym. Mater.*, in press.
- (5) Dolbier, W. R. *J. Fluorine Chem.* **2005**, *126*, 157–163.
- (6) Park, J. W.; Seo, Y. A.; Kim, I.; Ha, C. S. *Macromolecules* **2004**, *37*, 429–436.
- (7) Wormald, P.; Apperley, D. C.; Beaume, F.; Harris, R. K. *Polymer* **2003**, *44*, 643–651.
- (8) Nalwa, H. S. *Rev. Macromol. Chem. Phys.* **1991**, *31*, 341–432.
- (9) Wormald, P.; Ameduri, B.; Harris, R. K.; Hazendonk, P. *Solid State Nucl. Magn. Reson.* **2006**, *30*, 114–123.
- (10) Holstein, P.; Scheler, U.; Harris, R. K. *Polymer.* **1998**, *39*, 4937–4941.

- (11) Harris, R. K.; Monti, G. A.; Holstein, P. In *Solid State NMR of Polymers*; Ando, I., Asakura, T., Eds.; Elsevier: New York, 1998; pp 667–712.
- (12) Harris, R. K.; Monti, G. A.; Holstein, P. In *Solid State NMR of Polymers*; Ando, I., Asakura, T., Eds.; Elsevier: New York, 1998; pp 253–266.
- (13) Harris, R. K.; Jackson, P. *Chem. Rev.* **1991**, *91*, 1427–1440.
- (14) Brauniger, T.; Wormald, P.; Hodgkinson, P. *Monatsh. Chem.* **2002**, *133*, 1549–1554.
- (15) Bennet, A. E.; Rienstra, C. M.; Auger, M.; Lakshmi, K. V.; Griffin, R. G. *J. Chem. Phys.* **1996**, *103*, 1549–1554.
- (16) Ando, S.; Harris, R. K.; Hazendonk, P.; Wormald, P. *Macromol. Rapid Commun.* **2005**, *26*, 345–356.
- (17) Schmidt-Rohr, K.; Spiess, H. W. *Multidimensional Solid State NMR and Polymers*; Academic Press: London, 1994.
- (18) Ando, I.; Asakura, T. *Solid State NMR of Polymers*; Elsevier: New York, 1998.
- (19) Scheler, U. *Solid State Nucl. Magn. Reson.* **1998**, *12*, 9–13.
- (20) Ando, S.; Harris, R. K.; Holstein, P.; Reinsberg, S. A.; Yamauchi, K. *Polymer* **2001**, *42*, 8137–8151.
- (21) Ando, S.; Harris, R. K.; Reinsberg, S. A. *J. Magn. Reson.* **1999**, *141*, 91–103.
- (22) Harris, D. J.; de Azevedo, E. R.; Bonagamba, T. J. *J. Magn. Reson.* **2003**, *162*, 67–73.
- (23) Holstein, P.; Monti, G. A.; Harris, R. K. *Phys. Chem. Chem. Phys.* **1999**, *1*, 3549–3555.
- (24) Fyfe, C. A.; Rudin, A.; Tchir, W. *Macromolecules* **1980**, *13*, 1320–1322.
- (25) Hu, J. Z.; Taylor, C. M. V.; Pugmire, R. J.; Grant, D. M. *J. Magn. Reson.* **2001**, *152*, 7–13.
- (26) Mao, J. D.; Schmidt-Rohr, K. *J. Magn. Reson.* **2003**, *162*, 217–227.
- (27) Opella, S. J.; Frey, M. H. *J. Am. Chem. Soc.* **1979**, *101*, 5854–5856.
- (28) Cai, W. Z.; Schmidt-Rohr, K.; Egger, N.; Gerharz, B.; Spiess, H. W. *Polymer* **1992**, *34*, 267–276.
- (29) Clauss, J.; Schmidt-Rohr, K.; Adam, A.; Boeffel, C.; Spiess, H. W. *Macromolecules* **1992**, *25*, 5208–5214.
- (30) Spiegel, S.; Schmidt-Rohr, K.; Boeffel, C.; Spiess, H. W. *Polymer* **1993**, *34*, 4566–4569.
- (31) Egger, N.; Schmidt-Rohr, K.; Blumich, B.; Domke, W. D.; Stapp, B. *J. Appl. Polym. Sci.* **1992**, *44*, 289–295.
- (32) Buda, A.; Demco, D. E.; Bertmer, M.; Blumich, B.; Reining, B.; Keul, H.; Hocker, H. *Solid State Nucl. Magn. Reson.* **2003**, *24*, 39–67.
- (33) Liu, S. F.; Mao, J. D.; Schmidt-Rohr, K. *J. Magn. Reson.* **2002**, *155*, 15–28.
- (34) Bak, M.; Rasmussen, J. T.; Nielsen, N. C. J. *Magn. Reson.* **2000**, *147*, 296–330.
- (35) Mehring, M. *Principles of High Resolution NMR in Solids.*, 2nd ed.; Springer Verlag: Berlin, 1983.
- (36) Maple 11.0, Maplesoft, Waterloo Maple Inc., 1981–2007.
- (37) Hertzfeld, J.; Berger, A. E. *J. Chem. Phys.* **1980**, *73*, 6021–6030.

JP711489D